

# Controlled Partial Interpenetration in Metal-Organic Frameworks

Alan Ferguson,<sup>a</sup> Lujia Liu,<sup>a</sup> Stefanus J. Tapperwijn,<sup>a</sup> David Z. Perl,<sup>a</sup> Francois-Xavier Coudert,<sup>b</sup> Stijn Van Cleuvenbergen,<sup>c</sup> Thierry Verbiest,<sup>c</sup> Monique A. van der Veen<sup>d</sup> and Shane G. Telfer<sup>a,\*</sup>

<sup>a</sup> *MacDiarmid Institute for Advanced Materials and Nanotechnology, Institute of Fundamental Sciences, Massey University, Palmerston North, New Zealand.* <sup>b</sup> *Institut de Recherche de Chimie Paris, CNRS–Chimie ParisTech, 11 rue Pierre et Marie Curie, 75005 Paris, France.* <sup>c</sup> *University of Leuven, Celestijnenlaan 200D, Heverlee, Belgium.*

<sup>d</sup> *Catalysis Engineering, Applied Sciences, Delft University of Technology, Julianalaan 136, 2628 BL Delft, the Netherlands.*

*Email: s.telfer@massey.ac.nz*

**Abstract:** Interpenetration, the presence of multiple entwined lattices, is a common phenomenon in metal-organic frameworks (MOFs). In typical interpenetrated MOFs, the number of sublattices is an integer such as two or three. Here, we report MOFs with fractional degrees of interpenetration that can be controlled during synthesis. We also detail how the non-interpenetrated frameworks can be transformed into doubly-interpenetrated frameworks via progressively higher degrees of interpenetration in an ‘autocatenation’ process that involves no external reagents. This unique structural transformation maintains crystallinity and can be triggered thermally and by shear forces induced mechanically or by solvent evaporation. In addition to X-ray diffraction, nonlinear optical microscopy and theoretical calculations were implemented to characterize these materials and understand their remarkable properties. This study offers unprecedented insights into the growth mechanism and pliability of MOFs. It also presents a platform of materials whose adsorption properties will potentially benefit from the combination of high selectivity, rapid diffusion and ligand homochirality.

## Introduction:

Porous materials attain their molecular sieving, storage and catalytic properties by a combination of pore shape, size and surface functionality.<sup>[1-4]</sup> The question of how pore characteristics can be tuned to optimize these functional properties is critical. The chemical and structural diversity of metal-organic frameworks (MOFs) makes them an ideal platform to address this question.<sup>[5-6]</sup> To date, most emphasis has been placed on engineering the chemical characteristics of the pore surfaces. The influence of pore shape and size on functional behavior has received less attention, although it is clear that significant performance gains can be realized by tuning such framework metrics.<sup>[7-14]</sup>

Lattice interpenetration is a structural feature that impacts the size and shape of pores in MOFs while maintain their chemical characteristics.<sup>[15-20]</sup> Although interpenetration can reduce or altogether eliminate the porosity of framework materials, it can be employed as a tool to tailor pore metrics and modulate adsorption properties.<sup>[8,21-28]</sup> Interpenetrated MOFs are a common occurrence when permitted by the lattice size and topology. Methods to control this entanglement have been keenly pursued, and strategies such as using sterically-encumbered ligands,<sup>[29-31]</sup> low temperatures and concentrations during framework synthesis,<sup>[32]</sup> and bulky solvents<sup>[33-34]</sup> have emerged. In conventional MOFs, the degree of interpenetration adopts an integral value, for example two (in a doubly interpenetrated framework) or three (in a triply interpenetrated framework). The degree of interpenetration is usually fixed upon framework assembly, however in rare cases it has been shown that framework interpenetration in MOFs can be modified following synthesis by desolvation<sup>[35-38]</sup> or high-pressure intrusion of a liquid.<sup>[39]</sup> Here, we present two MOFs that exhibit exceptional interpenetration behavior. First, frameworks with partial degrees of interpenetration are observed in which the sites of a second lattice have non-integral (fractional) occupancy. The degree of interpenetration can be controlled during synthesis by the reaction time and by solvent composition. Second, the non-

interpenetrated lattices can be transformed into doubly-interpenetrated frameworks via progressively higher partial degrees of interpenetration. This *autocatenation* process preserves crystallinity and can be monitored and understood by X-ray diffraction, linear and nonlinear optical microscopy, and quantum chemistry calculations.

## Results and discussion

### *Synthesis of MUF-9 with controlled degrees of partial interpenetration*

Ligand **H<sub>2</sub>1** is a variant of 4,4'-biphenyldicarboxylic acid (H<sub>2</sub>bpdc) with phenyl substituents appended to a diazocine bridge (Fig. 1). To our knowledge, this ligand has not previously been used to construct MOFs. Due to twisting along its long axis **H<sub>2</sub>1** is chiral. Combining *rac*-**H<sub>2</sub>1** with Zn(NO<sub>3</sub>)<sub>2</sub> in a solvothermal reaction in N,N'-dimethylformamide (DMF) produces [Zn<sub>4</sub>O(*rac*-**1**)<sub>3</sub>] ( $\beta$ -MUF-9, MUF = Massey University Framework).  $\beta$ -MUF-9 belongs to a cubic crystal system (space group = *Pn*-3*m*) and features Zn<sub>4</sub>O secondary building units (SBUs) linked by the linear ligands into a primitive cubic (**pcu**) topology (Figs. 1, S34), as anticipated on the basis of related MOFs ligands.<sup>[40]</sup> Each ligand site is randomly occupied by one of the enantiomers of ligand **1** (Fig. S37).  $\beta$ -MUF-9 is doubly interpenetrated. The two lattices are related by crystallographic symmetry and the O atom of the Zn<sub>4</sub>O cluster of each lattice resides at the midpoint of the cube defined by its partner. The formation of an interpenetrated framework from ligand **1** is a counter-intuitive result given that bulky substituents typically produce noninterpenetrated lattices.<sup>[29-30,41]</sup>

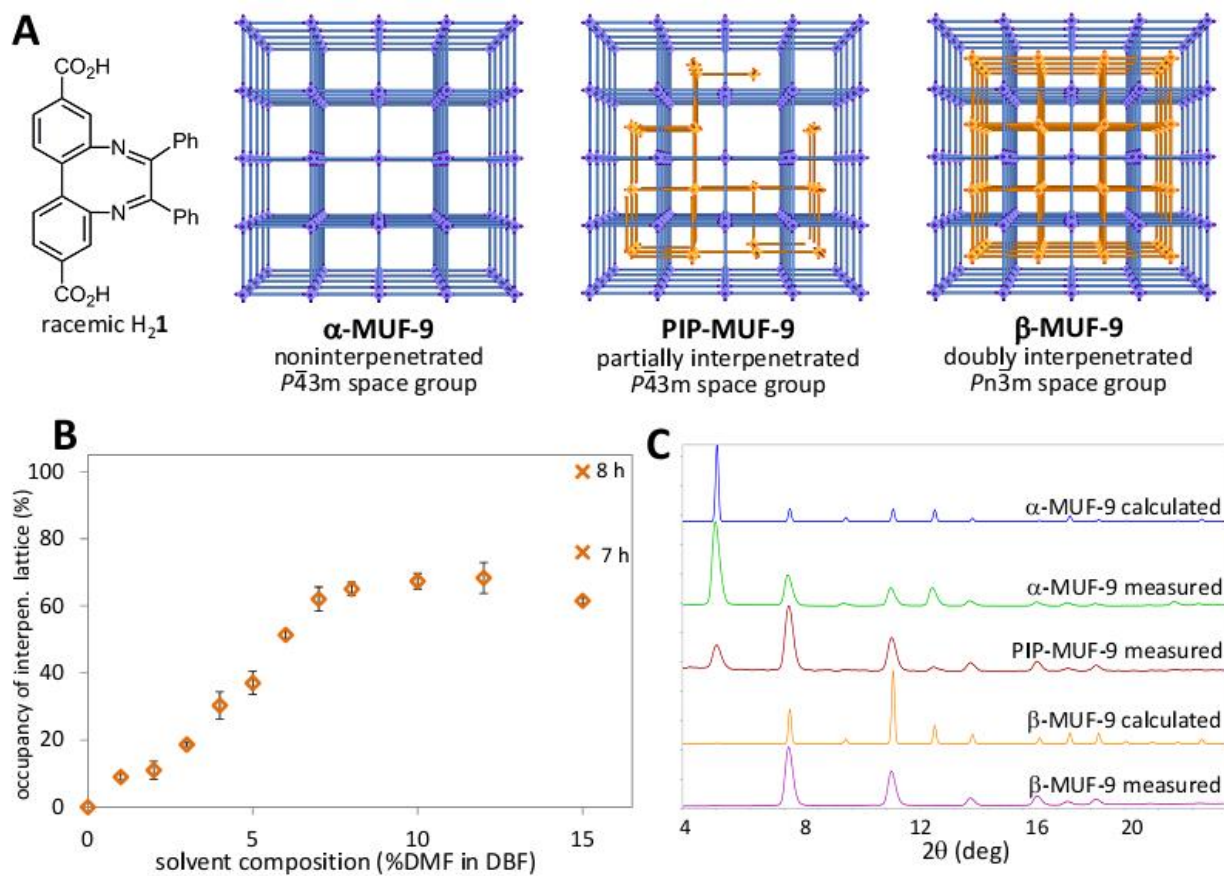


**Figure 1.** **A.** The nature of the solvent and the reaction time determine whether the combination of *rac*-H<sub>2</sub>1 with Zn(NO<sub>3</sub>)<sub>2</sub> at 85 °C produces  $\alpha$ -MUF-9 (noninterpenetrated), PIP-MUF-9 (partially interpenetrated), or  $\beta$ -MUF-9 (doubly interpenetrated). The structures of  $\alpha$ -MUF-9, PIP-MUF-9 and  $\beta$ -MUF-9 were determined by SCXRD. The interpenetrating lattice is shown in orange. In all frameworks the ligand sites are randomly occupied by one of the enantiomers of **1**. **B.** The use of DBF/DMF mixtures as the reaction solvent produces PIP-MUF-9. The level of interpenetration, given by the occupancy of the interpenetrating lattice determined by single crystal X-ray diffraction, is controlled by the amount of DMF in the solvent mixture. The orange diamonds represent the average level of interpenetration measured by independent SCXRD measurements on three crystals from the same batch after a reaction time of six hours, and the error bars indicate the standard deviation. The orange crosses correspond to the interpenetration level after reaction times of seven and eight hours with a 15% volume fraction of DMF. **C.** PXRD patterns (Cu $\alpha$  radiation) of  $\alpha$ -MUF-9 (experimentally measured and calculated from the

SCXRD structure), a selected example of PIP-MUF-9, and  $\beta$ -MUF-9 (experimentally measured and calculated from the SCXRD structure).

To explore the relationship between the composition of the reaction solvent and interpenetration in MUF-9 we carried out the reaction of  $H_2\mathbf{1}$  and  $Zn(NO_3)_2$  in other amide solvents (Tables 1, S1). Using N,N'-dibutylformamide (DBF) produces  $\alpha$ -MUF-9, the noninterpenetrated variant of MUF-9. This framework has close structural parallels to the individual lattices of  $\beta$ -MUF-9, and again each ligand site is randomly occupied by one of the two enantiomers of  $\mathbf{1}$  (Fig. S37). Reactions in N,N'-diethylformamide (DEF) over 16 h lead to interpenetrated  $\beta$ -MUF-9, while those in N,N'-isopropylformamide (DIF) and N-formylpiperidine (NFPip) generate a third phase,  $\gamma$ -MUF-9. Although  $\gamma$ -MUF-9 features the six-connected  $Zn_4O$  clusters observed in the  $\alpha$  and  $\beta$  phases, the clusters distort slightly to produce a **bsn** topology<sup>[42]</sup> (Fig. S39). It is noninterpenetrated and racemic with certain sites occupied specifically by one of the enantiomers and others occupied randomly by either enantiomer.

When small quantities of DMF were introduced into DBF we observed an intriguing outcome. Single-crystal X-ray diffraction (SCXRD) on the well-faceted blocks that deposit during solvothermal synthesis indicates that the original space group is maintained and that, remarkably, these crystals are a partially interpenetrated variant of MUF-9: the atomic sites of one lattice are fully occupied while those of a second network are fractionally occupied. The occupancy level of the second network corresponds to the percentage of unit cells, averaged over an entire crystal, that are doubly interpenetrated. This degree of partial interpenetration is designated as PIP-##-MUF-9 where ## is a percentage.

**Table 1.** The influence of the conditions on the outcome of the reaction of H<sub>2</sub>1 with Zn(NO<sub>3</sub>)<sub>2</sub>.

racemic H <sub>2</sub> 1			enantiopure H <sub>2</sub> 1		
Solvent <sup>a</sup>	Time (h)	Product	Solvent <sup>a</sup>	Time (h)	Product
<b>DBF</b>	6	$\alpha$ -MUF-9	<b>DBF</b>	16	$\alpha$ -MUF-10
<b>DBF</b>	134	PIP-90-MUF-9		70	$\alpha$ -MUF-10 <sup>b</sup>
<b>DBF/DMF</b>	6	PIP-MUF-9 <sup>c</sup>	<b>DBF/DMF</b>	16	PIP-MUF-10 <sup>c</sup>
<b>DEF</b>	2	PIP-MUF-9	<b>DEF</b>	16	$\gamma$ -MUF-10
	16	$\beta$ -MUF-9			
<b>DMF</b>	8	PIP-79-MUF-9	<b>DMF</b>	60	$\beta$ -MUF-10
	16	$\beta$ -MUF-9			
<b>DIF</b>	16	$\gamma$ -MUF-9	<b>DIF</b>	16	$\gamma$ -MUF-10
<b>NFPip</b>	16	$\gamma$ -MUF-9	<b>NFPip</b>	16	$\gamma$ -MUF-10
<b>NFPyr</b>	80	no MOF	<b>NFPyr</b>	120	$\gamma$ -MUF-10

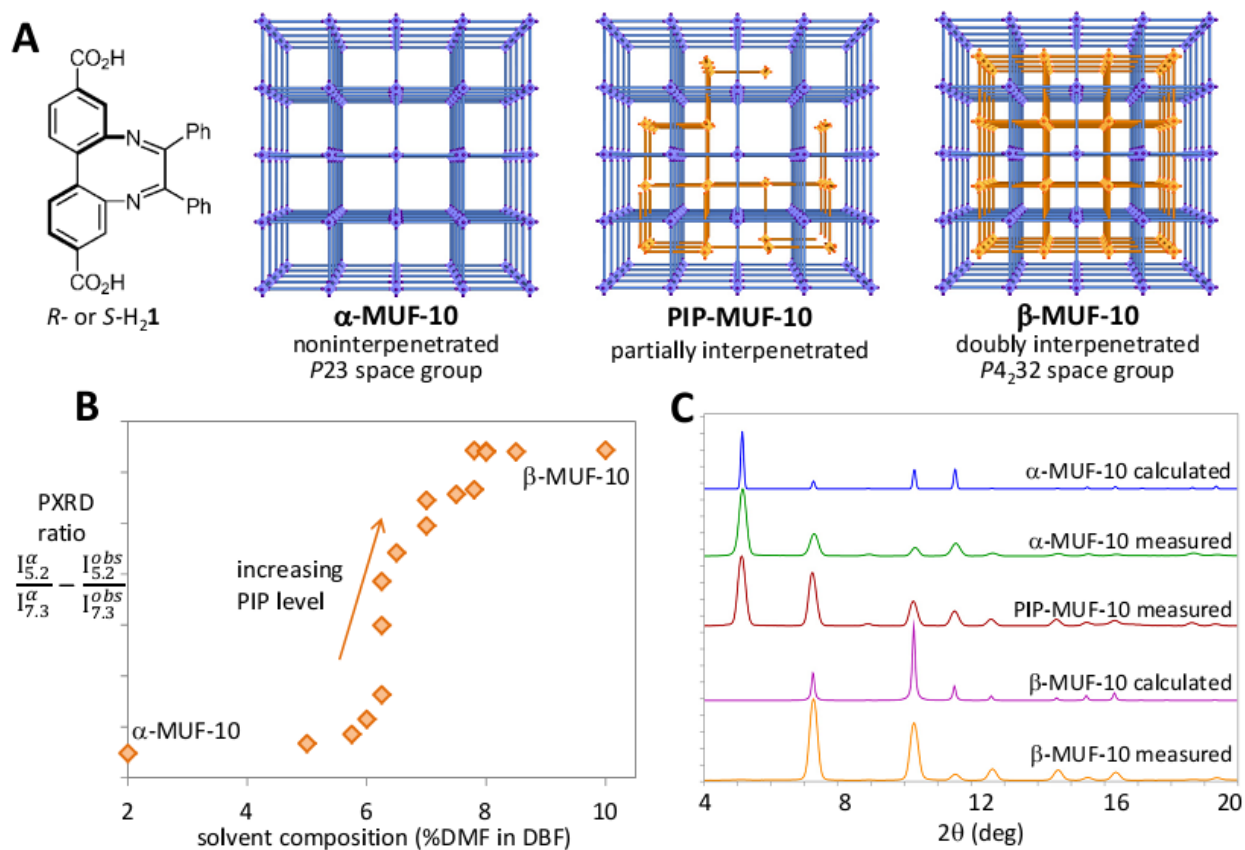
<sup>a</sup> DBF = N,N'-di-n-butylformamide; DEF = N,N'-diethylformamide; DMF = N,N'-dimethylformamide; DIF = N,N'-diisopropylformamide; NFPip = N-formylpiperidine; NFPyr = N-formylpyrrolidine <sup>b</sup> An additional, unknown phase also forms. <sup>c</sup> The level of partial interpenetration is controlled by the amount of DMF and the reaction time.

Figure 1b illustrates how the degree of partial interpenetration is controlled by the amount of DMF in the reaction medium following a set reaction time of six hours. Crystallographic datasets collected on more than 30 individual crystals (Table S3) portray a strong dependence of the interpenetration level on the fraction of DMF in the solvent mixture (Fig. 1b). It is noteworthy that the level of partial interpenetration in crystals from the same synthesis batch cluster within a narrow range. For example, three individual crystals grown from 5% DMF in DBF were found to have interpenetration levels between 33% and 39%. A limit to the level of interpenetration of ca. 65% that is reached over a period of six hours exists,<sup>[43]</sup> though as indicated by the crosses on Figure 1b extended reaction times further increase the PIP level to converge on  $\beta$ -MUF-9 (discussed in detail later). In addition to SCXRD, the degree of

interpenetration is reflected by the powder XRD (PXRD) patterns of bulk samples (Figs. 1c, S3). The (100) reflection at  $2\theta = 5.2^\circ$  ( $d = 17.2 \text{ \AA}$ ) is intense for  $\alpha$ -MUF-9 but systematically absent for  $\beta$ -MUF-9. For PIP-MUF-9, the degree of interpenetration correlates with a progressive decrease in the intensity of the (100) reflection relative to the (110) reflection at  $2\theta = 7.2^\circ$

Partial interpenetration can be viewed as an unusual case of structural disorder.<sup>[45]</sup> It has previously been reported in a seminal publication in 2012 that described NOTT-202, an indium-carboxylate MOF. The second lattice of this material has an occupancy of 75%.<sup>[44]</sup> However, the non-interpenetrated variant of NOTT-202 was not observed, and only one level of partial interpenetration was achieved. MUF-9 has advantages over NOTT-202 by providing straightforward and controlled access to materials with virtually any degree of interpenetration between zero and one.

MUF-10 is the enantiopure counterpart of MUF-9, which can be synthesized using resolved *R*-H<sub>2</sub>**1** or *S*-H<sub>2</sub>**1** (Fig. 2, Tables 1, S2). A high energy barrier<sup>[46]</sup> prevents racemization of the ligand during MOF synthesis. Using DMF as the reaction solvent produces the doubly-interpenetrated framework  $\beta$ -MUF-10, whereas DBF leads to the noninterpenetrated phase  $\alpha$ -MUF-10.  $\alpha$ -MUF-10 defines a regular **pcu** lattice, two perfectly offset copies of which are present in  $\beta$ -MUF-10. Switching to DEF as the solvent generates  $\gamma$ -MUF-10, a noninterpenetrated framework with a **bsn** topology. Several other formamide solvents – DIF, NFPip, NFPyr (N-formylpyrrolidine) – were also found to produce  $\gamma$ -MUF-10 (Fig. S13). All ligand sites in the MUF-10 series are occupied by linkers with the same handedness (Fig. S38), and, as mandated by their homochirality, all frameworks belong to chiral space groups (Table S4).



**Figure 2.** **A.** The solvent composition and reaction time determine whether the combination of *R*- or *S*-H<sub>2</sub>1 with Zn(NO<sub>3</sub>)<sub>2</sub> at 85 °C produces α-MUF-10 (noninterpenetrated), PIP-MUF-10 (partially interpenetrated), or β-MUF-10 (doubly interpenetrated). The structures of α-MUF-10 and β-MUF-10 were determined by SCXRD, while the structures of PIP-MUF-10 were deduced by PXRD. The linkers in each framework are enantiopure. **B.** The rise in the level of interpenetration in PIP-MUF-10 with increasing amounts of DMF in the DBF reaction solvent is indicated by the relative intensities ( $I^{obs}$ ) of the peaks at 5.2° and 7.3° in the observed PXRD pattern with respect to the intensities observed for α-MUF-10 ( $I^{\alpha}$ ). **C.** PXRD patterns (Cu<sub>α</sub> radiation) of α-MUF-10 (experimentally measured and calculated from the SCXRD structure), an example PIP-MUF-10, and β-MUF-10 (experimentally measured and calculated from the SCXRD structure).



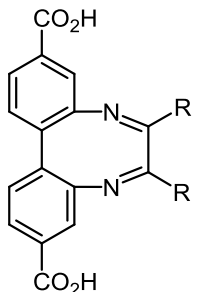
In parallel with our observation on MUF-9, partial degrees of interpenetration can be generated in MUF-10 by using small amounts of DMF in DBF as the reaction medium (Fig. 2b). The crystal quality of partially interpenetrated MUF-10 did not permit SCXRD to be used to determine the fractional occupancy of the second lattice. However, in a similar fashion to MUF-9, the (100) reflection is extinguished by the presence of the second lattice therefore it diminishes markedly in intensity with increasing degrees of partial interpenetration (Figs. 2c, S10).

We also examined the effect of reaction time on the level of interpenetration in MUF-9 and MUF-10 (Tables 1, S1, S3). For MUF-9, X-ray diffraction revealed that crystals formed at the onset of crystallization in DMF (after eight hours) and DEF (after two hours) are partially interpenetrated (79% for DMF and 71% for DEF, Tables 1 and S3, Fig. S5). Prolonging the reaction time allows the second network to further infiltrate the void space of the first, eventually delivering  $\beta$ -MUF-9 as the sole product in both solvents. In DBF, SCXRD snapshots show that framework growth proceeds in a related way: the initially-formed  $\alpha$ -MUF-9 crystals are progressively converted to PIP-90-MUF-9 over a period of about one week (Table S3). The foregoing results lead to the conclusion that the solvent system independently tunes the growth rates of the first and second lattices. Their growth rates are quite similar in DMF, therefore when crystals reach a size amenable to SCXRD the level of interpenetration is already high. The growth rates appear to be quite different in DBF: the first lattice crystallises within hours, however the growth rate of the interpenetrating network is much slower. Adding DMF to the DBF accelerates the growth of this second sublattice.

In contrast to MUF-9,  $\alpha$ -MUF-10 completely resists interpenetration when grown in DBF even after prolonged reaction times. Instead, a new (unknown) phase appears in the reaction mixture after two days (Fig. S12). In DMF/DBF mixtures, the PIP-MUF-10 crystals that are formed in the early stages of the reaction gradually convert to  $\beta$ -MUF-10 (Fig. S11). Thus, as for MUF-9,

premeditated PIP levels in MUF-10 simply by selecting the appropriate solvent composition and reaction time.

**Table 2.** MOFs synthesised using ligands H<sub>2</sub>2, H<sub>2</sub>3, and H<sub>2</sub>4.

	Ligand	MOF
	H <sub>2</sub> 2, R = 4-methylphenyl	MUF-11, [Zn <sub>4</sub> O(2) <sub>3</sub> ]
	H <sub>2</sub> 3, R = 4-bromophenyl	MUF-12, [Zn <sub>4</sub> O(3) <sub>3</sub> ]
	H <sub>2</sub> 4, R = methyl	MUF-14, [Zn <sub>4</sub> O(4) <sub>3</sub> ]

To probe the impact of modifications to the ligand structure on the propensity for partial interpenetration we synthesized MUF-11, MUF-12 and MUF-14 (Table 2). H<sub>2</sub>2 and H<sub>2</sub>3 behave in a similar way to H<sub>2</sub>1: heating with Zn(NO<sub>3</sub>)<sub>2</sub> in DBF produces MUF-11 and MUF-12 crystals, respectively, that are noninterpenetrated when initially formed (~3 hours) but become progressively more interpenetrated over time (Figs. S14, S15). Both β-MUF-11 and β-MUF-12 can be obtained directly by synthesis in DMF, and analysis by SCXRD reveals very close structural similarities to MUF-9. Monitoring the formation of MUF-14 in DEF demonstrates that in the early stages of the reaction α-MUF-14 is produced. Over time, PIP-MUF-14 appears and the level of partial interpenetration increases as a function of the reaction time (Fig. S16). These experiments significantly broaden the scope of this study and promise a platform of materials with both tunable chemical characteristics and levels of partial interpenetration.

MOFs with controlled degrees of interpenetration have the potential to be useful in applications where materials that allow both rapid mass transport and high surface area can avoid the trade-off that typically exists between capacity and selectivity. Akin to hierarchical zeolites,<sup>[47-48]</sup> the small pockets defined by the regions of interpenetration provide scope for discriminating

molecular guests, while the large noninterpenetrated void spaces will speed up diffusion. In addition, adsorption sites of high polarity (due to dangling bonds) and complex geometries will be created at the propagation fronts of the interpenetrating lattice. Amongst other applications, the homochirality of MUF-10 provides a means of discriminating the enantiomers of chiral guest molecules such as pharmaceuticals and natural products.<sup>[49]</sup> While a comprehensive examination of guest uptake by MUFs 9-14 is still in progress, TGA and <sup>1</sup>H NMR spectroscopy on MUF-9 and MUF-10 (Figs. S47-56) indicate that the noninterpenetrated frameworks incorporate more solvent than their doubly-interpenetrated counterparts, as expected on the basis of their larger void volumes. The degree of interpenetration also dictates their ability to adsorb acridine orange from solution. Deep coloration of  $\alpha$ -MUF-9 and  $\alpha$ -MUF-10 crystals indicates a high loading of the dye (Figs. S40, S45). As the degree of interpenetration in MUF-9 increases its capacity for acridine orange uptake is reduced (Figs. S41-42), and it is excluded from the smaller pores of  $\beta$ -MUF-9 and  $\beta$ -MUF-10 (Figs. S43, 45).

### ***Autocatenation of $\alpha$ -MUF-9 and $\alpha$ -MUF-10***

In a remarkable process that we term *autocatenation*  $\alpha$ -MUF-9 can be transformed into its doubly interpenetrated analogue via progressively degrees of partial interpenetration in a single-crystal-to-single-crystal phase transition<sup>[50]</sup> (Fig. 3). No external reagents are involved and the process is irreversible. Autocatenation can be triggered in at least three ways: thermally, by crystal desolvation, and by mechanical shearing. In the thermal process, crystals of  $\alpha$ -MUF-9 heated to 85 °C in DMF maintain their external appearance over the course of two days but shrink in size. The crystal volume reduces by around 50% over the course of autocatenation (Figs. 3b, S20), which squares with the expected twofold increase in density. A well-resolved set of X-ray diffraction spots, which corresponds to the 17.2 Å cubic unit cell of MUF-9, is

maintained by the crystals. The increase in intensity of diffraction at high  $2\theta$  angles indicates that the structural regularity of the lattice improves as the degree of interpenetration increases (Fig. 3c). At any point during the transformation the degree of interpenetration can be determined by SCXRD (Fig. 3d, Table S3).

Heating crystals of  $\alpha$ -MUF-10 over a period of several days at 85 °C in DMF also induces autocatenation, producing  $\beta$ -MUF-10 (Figs. S26-31). A general trend in the rate of autocatenation emerges for both MUF-9 and MUF-10. An initial period where the degree of interpenetration rises slowly is followed by a more rapid change to deliver the fully interpenetrated framework (Figs. 3d, S27). Small quantities of water,  $\text{Zn}(\text{NO}_3)_2$ , and  $\text{H}_2\mathbf{1}$  added to the DMF solution all accelerate the autocatenation of  $\alpha$ -MUF-10. Further notable observations include: (i) Distinct differences in autocatenation rates exist amongst individual  $\alpha$ -MUF-9 crystals heated in DMF for the same period of time (Fig. 3d). (ii) Directly-synthesized PIP-MUF-9 converts to  $\beta$ -MUF-9 by heating in DMF (Fig. S17). (iii) Autocatenation of  $\alpha$ -MUF-9 and PIP-MUF-9 occurs upon heating in DEF (Figs. S18-18), however no changes are detectable upon heating in DBF (Fig. S22) nor in DBF/DMF 80/20 (Table S3). (iv) A dissolution-reprecipitation mechanism for the phase transition was ruled out by monitoring the interpenetration changes of a solitary crystal in a large volume of DMF, where the effects of dilution would preclude regrowth of the MOF. Furthermore, no free ligand is detectable in the supernatant during autocatenation (Fig. S21). (v) The propensity of  $\alpha$ -MUF-9 to autocatenate is not shared by  $\gamma$ -MUF-9 (Fig. S25).

The autocatenation of  $\alpha$ -MUF-9 can also be induced by the escape of occluded DMF from the pores of the noninterpenetrated lattice. Here, we monitored the conversion by SCXRD, which showed PIP-77-MUF-9 to be present after 100 minutes of drying and then  $\beta$ -MUF-9 after a further 100 minutes (Table S3). Optical microscopy reveals cloudy pseudomorphs of the crystals

that are reduced in volume by around 25% (Fig. S23). This volume decrease is lower than the 50%, expected, owing to incomplete interpenetration (see NLO microscopy later) and the possible formation of mesoscale voids that are hinted at by the loss of transparency. Autocatenation of  $\alpha$ -MUF-10 is also induced by the loss of DMF from the framework pores. Evidence for this phase change comes from changes in PXRD patterns (Fig. S32), and a reduction in the crystal volume of ca. 45% (Fig. S33), which is close to the ideal value of 50%. In the case of MUF-10 the crystals maintain both their external form and optical transparency.

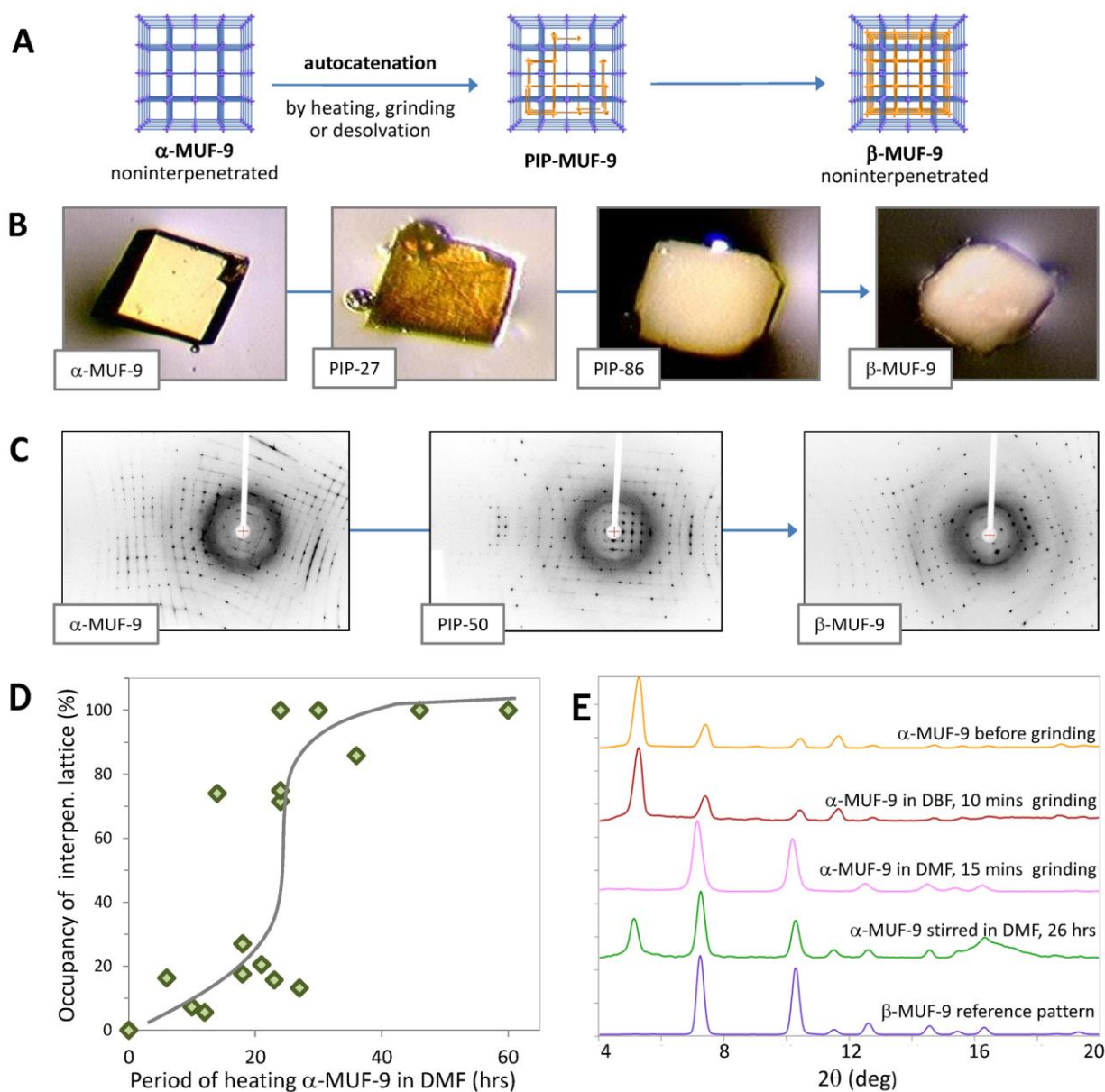


**Figure 3.** A.  $\alpha$ -MUF-9 can be converted to  $\beta$ -MUF-9 by a single-crystal-to-single-crystal autocatenation process. Crystals with progressively higher degrees of partial interpenetration are produced along the pathway from  $\alpha$ -MUF-9 to  $\beta$ -MUF-9. B. Optical micrographs of a crystal undergoing this conversion by heating to 85 °C in DMF. C. X-ray diffraction images demonstrate that structure is maintained during thermally-induced autocatenation. D. For thermal autocatenation, the level of interpenetration, as determined by the occupancy of the interpenetrating lattice determined by single crystal X-ray diffraction, is controlled by the heating time. A degree of variability is observed between individual crystals heated for the same length of time. The grey line is a guide for the eye. E. PXRD patterns ( $\text{Cu}_\alpha$  radiation) of  $\alpha$ -MUF-9 after grinding in a mortar and pestle in DBF, which produces no structural changes (red trace), and after grinding in DMF, which results in conversion to  $\beta$ -MUF-9 (pink trace). Mechanical grinding using a magnetic stir-bar produces PIP-MUF-9 (green trace).

Mechanochemical forces exert a similar effect to desolvation. For example, grinding crystals of  $\alpha$ -MUF-9 suspended in DMF, using either a conventional mortar and pestle or a magnetic stir-bar, produced  $\beta$ -MUF-9 via progressively higher degrees of partial interpenetration (Figs. 3e, S24). Conversely, isotropic compression at pressures of up to 0.5 GPa left  $\alpha$ -MUF-9 unchanged. Related examples of a postsynthetic change in interpenetration state have been reported for MOF-123,<sup>[37]</sup>  $[\text{Zn}_2(\text{ndc})_2(\text{bpy})]$ ,<sup>[36]</sup> and  $[\text{Cd}(\text{bdc})(\text{bpy})]$ <sup>[35]</sup> (ndc = 2,6-naphthalenedicarboxylate; bpy = 4,4'-bipyridine; bdc = 1,4-benzenedicarboxylate). In the case of MOF-123, autocatenation is triggered by heating the framework to expel coordinated DMF molecules. The process is reversed upon exposure to DMF. In  $[\text{Zn}_2(\text{ndc})_2(\text{bpy})]$ , a doubly-interpenetrated framework converts into its triply-interpenetrated analogue by desolvation, while  $[\text{Cd}(\text{bdc})(\text{bpy})]$  switches from being noninterpenetrated to doubly-interpenetrated. **It has also been established that**

coordination bonds can be cleaved *en masse* in to alter the dimensionality of coordination polymers,<sup>[50-51]</sup> which is often correlated with solvent loss.<sup>[52]</sup> MUF-9 and MUF-10 go beyond these materials by showing that this transformation can be effected in an archetypal Zn<sub>4</sub>O-carboxylate MOF and triggered by a range of stimuli. Intermediate frameworks with partial degrees of interpenetration can be isolated and characterized along the autocatenation pathway for the first time.

### ***Nonlinear optical microscopy***

We interrogated crystals of MUF-9 with various levels of interpenetration using nonlinear optical microscopy. Second harmonic generation (SHG) microscopy serves as a sensitive probe of local crystal organization since its efficiency depends strongly on point group symmetry.<sup>[53-54]</sup> SHG is forbidden in centrosymmetric materials thus SHG microscopy provides contrast between the noncentrosymmetric ( $\alpha$ -MUF-9) and centrosymmetric phases ( $\beta$ -MUF-9). As expected,  $\alpha$ -MUF-9 produces a bright SHG response (Fig. 4a).<sup>[55]</sup> In contrast, no signal emerges from  $\beta$ -MUF-9 (Fig. 4d), which confirms the inversion symmetry deduced by X-ray crystallography. SHG responses that are weaker than for  $\alpha$ -MUF-9 due to the increased fraction of the lattice that is centrosymmetric are observed for PIP-MUF-9 (Figs 4b, 4c). Two-photon fluorescence (2PF) microscopy, on the other hand, images materials regardless of their point group symmetry. 2PF signals are generated by both  $\alpha$ -MUF-9 and  $\beta$ -MUF-9, although they are significantly weaker for the latter.

Although X-ray crystallography gives a reliable estimate of the overall level of interpenetration in PIP-MUF-9 crystals it provides an averaged picture and cannot map interpenetrated regions with high resolution. In contrast, SHG microscopy is an ideal tool for determining whether the interpenetrating lattice is present uniformly throughout MUF-9 crystals or confined to certain

spatial zones. The synthesis of MUF-9 in DBF was monitored by SHG microscopy over a period of days as the interpenetrating lattice grows in (Fig. S58). For PIP-15-MUF-9, the SHG response was initially observed to be uniform, which implies that growth of the second framework is not localized in a specific crystal region. Over time, the level of partial interpenetration increases and the 2PF and SHG responses becomes patchier and domains of several microns in size appear (e.g. PIP-35-MUF-9 in Fig. 4b). We ascribe this inhomogeneity to crystal zones with differing degrees of interpenetration. As expected, for the more highly interpenetrated crystals an increased spatial uniformity is coupled to an overall attenuation of the SHG signal (Fig. S58). The 2PF and SHG responses from PIP-40-MUF-9 crystals grown directly in DMF/DBF is patchy across individual crystals, revealing the existence of zones of a few microns in size with differing degrees of interpenetration (Fig. 4c).

Upon autocatenation induced by evaporation of DMF from  $\alpha$ -MUF-9 the SHG signal intensity from the crystals decreases steadily, as anticipated (Figs. S59, S60). This signal reduction occurs uniformly throughout the crystals, implying the interpenetrated crystal zones are spatially homogeneous. The SHG response persists to a minor degree even following complete desolvation due to small localized noncentrosymmetric pockets where the lattice is noninterpenetrated (Fig. 4e).



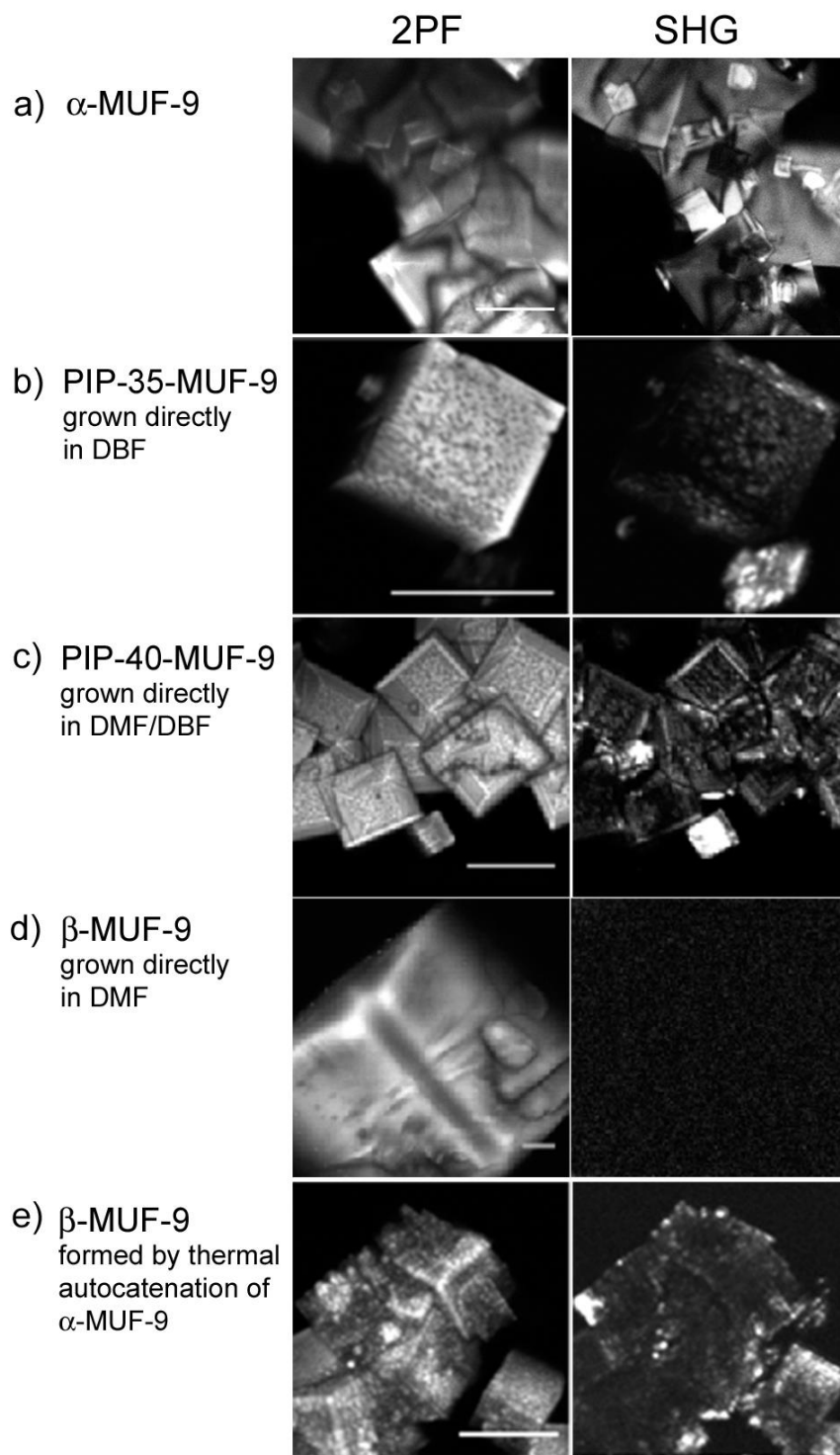


**Figure 4.** Second harmonic generation (SHG) and two-photon fluorescence (2PF) images of MUF-9 crystals with various levels of interpenetration produced by different methods. The SHG response of the crystals drops with increasing levels of interpenetration, which is consistent with the difference in symmetry between  $\alpha$ -MUF-9 (noncentrosymmetric) and  $\beta$ -MUF-9 (centrosymmetric). The length of the scale bar is set to 30  $\mu\text{m}$  in the 2PF images.

### *Theoretical characterization*

In order to better understand the unique interpenetration behavior of MUF-9 and MUF-10, we performed quantum chemical calculations at the DFT level on two guest-free models of MUF-10. These models are herein referred to as  $\alpha$ -MUF-10 and  $\beta$ -MUF-10 to distinguish them from the crystallographic structures.<sup>[56]</sup> For the purpose of comparison, we also performed calculations on  $\gamma$ -MUF-10, as well as two archetypical MOFs with the **pcu** topology, IRMOF-9 (doubly interpenetrated  $[\text{Zn}_4\text{O}(\text{bpdc})_3]$ ) and IRMOF-10 (non-interpenetrated  $[\text{Zn}_4\text{O}(\text{bpdc})_3]$ ). All structures were fully energy-minimized, with the resulting coordinates appended as ESI and their crystallographic parameters summarized in Table S5.

The calculations confirm that evacuated  $\alpha$ -MUF-10 is a metastable phase with respect to  $\beta$ -MUF-10, with an interpenetration enthalpy of 62.9 kJ/mol per  $\text{Zn}_4\text{O}$  unit. This is much larger than the interpenetration enthalpy for the conversion of IRMOF-10 to IRMOF-9, which we calculate to be 24.0 kJ/mol. This difference can be ascribed to the significant interligand contacts between the pendant phenyl rings the side chains of the ligands in MUF-10 (Fig. S35). We also calculated the structure and relative energy of the porous  $\gamma$ -MUF-10 structure without its coordinated water and formamide molecules: it falls slightly (9.1 kJ/mol) below the  $\alpha$ -MUF-10 phase, being intermediate between  $\alpha$ -MUF-10 and  $\beta$ -MUF-10.

Calculations of the second-order elastic tensors can shed light on the mechanical properties of MOF lattices,<sup>[57]</sup> in particular their mechanical stability and their propensity for structural transitions upon mechanical compression, shear forces<sup>[58]</sup> or guest evacuation.<sup>[59]</sup> The full tensors of  $\alpha$ - and  $\beta$ -MUF-10 are given in Table S6-7, and their calculated mechanical properties are summarized in Table S8. As calculated for related porous MOFs,<sup>[60]</sup>  $\alpha$ -MUF-10 is extremely soft, with an average Young's modulus of 3.7 GPa and a shear modulus of 1.3 GPa. In addition, it shows a highly anisotropic elastic behavior characteristic of flexible MOFs, so-called *soft*

*porous crystals*, that undergo stimuli-induced structural transitions.<sup>[61-64]</sup> The softest mode of the structure corresponds to an extremely low modulus of 0.13 GPa for shearing along the (122) direction of the  $\alpha$ -MUF-10 model (see movie in ESI), which corresponds to a rhombohedral shear of the cubic  $\alpha$ -MUF-10 structure. The calculated average bulk modulus is 6.8 GPa, significantly higher than the low shear modulus, which is in accord with experiments showing that the noninterpenetrated structures are unchanged by isotropic compression at moderate pressures.

In comparison to  $\alpha$ -MUF-10, the calculated elastic properties of the interpenetrated  $\beta$ -MUF-10 depict a much stiffer material, with a bulk modulus of 11.7 GPa, average Young's modulus of 8.9 GPa and shear modulus of 3.2 GPa. This is consistent with the generally observed correlation between elastic properties and framework density, often as seen as a function of guest loading and pore topology,<sup>[58,65]</sup> and as previously calculated in the specific case of MOF-14.<sup>[66]</sup> In addition to being stiffer than the noninterpenetrated phase,  $\beta$ -MUF-10 also shows much lower anisotropy of its elastic properties, as is typical for inflexible MOFs. Its softest deformation mode is also a shearing mode, but its elastic modulus of 1.0 GPa indicates a mechanical stability that is an order of magnitude higher than  $\alpha$ -MUF-10.

The insights provided by these calculations are consistent with related literature reports and allow us draw conclusions regarding the mechanism for the instability of  $\alpha$ -MUF-9 and  $\alpha$ -MUF-10 (see later) by quantitatively evaluating the lowest shear modulus in both structures. This tensorial analysis, although performed on the MIL-53 and some other flexible MOFs,<sup>[57,67]</sup> is used here for the first time in evaluating the impact of interpenetration.

### ***Partial interpenetration, framework growth, and autocatenation behaviour***

Interpenetration in MOFs is a well-studied phenomenon, however partial interpenetration has only been reported on one previous occasion.<sup>[44]</sup> Why is partial interpenetration such a rare

occurrence yet readily manifest in the MOFs reported herein? Since partially interpenetrated lattices will have linkers with donor groups that are not coordinated to metal ions and/or open metal sites on their metal clusters, it is likely that they incur a significant energy penalty. This must be offset by energy gains elsewhere for partially interpenetrated MOFs to be stable enough to be observed. Bulky ligand substituents are generally considered to suppress interpenetration, however, in the case of MUF-9-14, the ligands are extend laterally from their main axis to the point where they engage in noncovalent contacts with the partner sublattice (Figs. S35, S36). Drawing on both our experimental and computational results, we propose that these contacts provide the stability gains that enable partial interpenetration. These interactions are enabled by distinctive structural characteristics of linkers **1** – **4**, which explains why partial interpenetrations has not previously been observed in the very well-studied<sup>[29-30,34,68]</sup> family of IRMOF-9 derivatives.

The ability to isolate partially interpenetrated MOFs relies on the growth rate of the host lattice to significantly exceed that of the interpenetrating lattice. In this way the host lattice forms before its pores are infiltrated by the second network. The composition of the solvent is a key variable in discriminating the sublattice growth rates. Bulky solvents slow the development of the interpenetrating lattice so that crystals with any desired level of partial interpenetration to be conveniently harvested. This correlation between ligand structure, the solvent, and the degree of partial interpenetration provides the basis for the rational development of a broad range of partially interpenetrated MOFs.

A long-standing question in MOF chemistry has been whether the sublattices of interpenetrated frameworks grow in a stepwise or simultaneous fashion. Such mechanistic questions are typically difficult to address. Now, from our observations on MUF-9 it is clear that a stepwise growth mechanism can operate to produce an interpenetrated phase via an initially-formed noninterpenetrated phase. This process follows Ostwald's rule of stages<sup>[69-70]</sup> in that a metastable

phase cascades down to the final thermodynamically preferred product, in this case via a series of intermediate partially interpenetrated states.

A third, hitherto unrecognized, growth mechanism can also generate interpenetrated MOFs. Thermal autocatenation of MUF-9 and MUF-10 reveals that the components of a noninterpenetrated MOF can rearrange into an interpenetrated lattice. On this basis we speculate that, in certain cases, interpenetrated frameworks may develop by concurrent processes of lattice growth and autocatenation. This mechanism could produce interpenetrated MOFs whose direct formation is inhibited by low reaction temperatures or concentrations or where the transport of fresh reagents, such as bulky ligands, through the pores of a growing framework is restricted. Our contrasting observations on the growth of MUF-9 in various solvents are consistent with this mechanism.  $\beta$ -MUF-9 is produced in DMF and DEF while level of partial interpenetration plateaus at 80% even after prolonged growth in DBF. In DMF and DEF thermal autocatenation is a viable process and interpenetrating lattices reach full occupancy over time. This can be achieved by an autocatenation mechanism filling in the non-interpenetrated regions without the need to transport in fresh framework components. Conversely, since thermal autocatenation is not possible in DBF, the formation of the interpenetrating lattice in crystals grown in this solvent relies solely on diffusion of fresh components through the pores of the parent network. In this way, growth of the second lattice is self-inhibiting – access of free ligand to the interior of the crystal will progressively more difficult as the degree of interpenetration rises – therefore certain crystal regions remain non-interpenetrated.

Autocatenation of MUF-9 and MUF-10 reveals a surprising degree of pliability for  $Zn_4O$ -carboxylates MOFs in that single crystallinity is maintained during a structural reconfiguration that requires large numbers of metal-ligand bonds to be transiently cleaved. Our observations indicate that the genesis and propagation of the interpenetrating lattice has parallels with the conventional model of crystal nucleation. Since the degree of autocatenation is not a smooth

function of heating time (Fig. 3d) it appears to be triggered in individual crystals at different times. This is consistent with stochastic nucleation of the interpenetrating sublattice. The SHG microscopy images imply that numerous nucleation sites develop throughout the crystals in a spatially uniform manner. In thermal autocatenation, these nucleation sites develop over the course of an induction period, during which the interpenetration level rises only slowly, which is followed by a sharp rise in the degree of interpenetration as the second lattice becomes more extensive.

The observed propensity for MUF-9 and MUF-10 to undergo autocatenation is explained by calculations that show that noninterpenetrated lattices have very low shear moduli. Large shear forces and internal stresses are produced by heating, grinding, or evaporation of the solvent trapped in MOF pores. It is commonly observed that MOFs<sup>[71-72]</sup> are mechanically unstable towards such forces and tend to collapse to a dense and/or amorphous material upon solvent escape. In the case of MUF-9 and MUF-10, shear forces propel the frameworks along an autocatenation trajectory that links the noninterpenetrated and double interpenetrated frameworks. The stabilizing noncovalent interactions that develop in interpenetrated regions of the crystal act to lower the energy barrier to this reconfiguration. *These observations will assist the *in silico* discovery of other frameworks that have a propensity for autocatenation.*

## ***Conclusion***

*We have shown that partial interpenetration in a series of metal-organic frameworks can be precisely controlled, and that autocatenation can transform metastable noninterpenetrated frameworks into their doubly interpenetrated counterparts via progressively higher degrees of partial interpenetration. These remarkable observations offer unique perspectives on the structure, reactivity, and growth mechanisms of MOFs. Ongoing investigations are aimed at exploring the guest adsorption properties of this platform of porous materials. These frameworks*

feature identical pore chemistries but different channel systems, and the partially interpenetrated regions of the crystals are expected to provide selective binding pockets while the noninterpenetrated regions will enable rapid diffusion. Amongst other applications, the homochirality of MUF-10 provides a means of discriminating the enantiomers of chiral guest molecules.

**Acknowledgements:** We are grateful to the RSNZ Marsden Fund and the MacDiarmid Institute for financial support, David Lun for technical assistance, Dr. Suresh Narayamaswamy and Chris Lepper for help with the high pressure experiments, and the staff of the Manawatu Microscopy and Imaging Centre at Massey University. FXC acknowledges computing time on HPC platforms provided by a GENCI (grant x2015087069), and SVC and TV acknowledge financial support from the Hercules foundation and the FWO-Flanders (research project G.0927.13).

**Author contributions:** AF, LL, DP, SJT, SvC and SGT designed the experiments, carried out the experimental work, and interpreted the experimental data. FXC performed the theoretical calculations and analyzed the results. SGT coordinated the writing of the manuscript with input from all authors.

**Electronic Supplementary Information:** Experimental methods, computational and crystallographic data, and additional details.

## References:

1. 'Ordered Porous Materials for Emerging Applications,' M. E. Davis, *Nature* **2002**, *417*, 813.
2. 'Advances in Microporous and Mesoporous Solids,' A. Stein, *Adv. Mater.* **2003**, *15*, 763.
3. 'Design and Preparation of Porous Polymers,' D. Wu, F. Xu, B. Sun, R. Fu, H. He and K. Matyjaszewski, *Chem. Rev.* **2012**, *112*, 3959.
4. 'Covalent Organic Frameworks,' X. Feng, X. Ding and D. Jiang, *Chem. Soc. Rev.* **2012**, *41*, 6010.
5. 'The Chemistry and Applications of Metal-Organic Frameworks,' H. Furukawa, K. E. Cordova, M. O'Keeffe and O. M. Yaghi, *Science* **2013**, *341*, 974.
6. 'Crystal Engineering, Structure-Function Relationships, and the Future of Metal-Organic Frameworks,' M. D. Allendorf and V. Stavila, *CrystEngComm* **2015**, *17*, 229.

7. 'Targeted Manipulation of Metal–Organic Frameworks to Direct Sorption Properties,' A. Schneemann, S. Henke, I. Schwedler and R. A. Fischer, *ChemPhysChem* **2014**, *15*, 823.
8. 'Porous Metal–Organic Frameworks for Gas Storage and Separation: What, How, and Why?,' B. Li, H.-M. Wen, W. Zhou and B. Chen, *J. Phys. Chem. Lett.* **2014**, *5*, 3468.
9. 'A Family of Porous Lonsdaleite-E Networks Obtained through Pillaring of Decorated Kagomé Lattice Sheets,' A. Schoedel, W. Boyette, L. Wojtas, M. Eddaoudi and M. J. Zaworotko, *J. Am. Chem. Soc.* **2013**, *135*, 14016.
10. 'Pore Surface Engineering of Microporous Coordination Polymers,' S. Kitagawa, S.-i. Noro and T. Nakamura, *Chem. Commun.* **2006**, 701.
11. 'Systematic Ligand Modulation Enhances the Moisture Stability and Gas Sorption Characteristics of Quaternary Metal–Organic Frameworks,' L. Liu and S. G. Telfer, *J. Am. Chem. Soc.* **2015**, *137*, 3901.
12. 'Programmed Pore Architectures in Modular Quaternary Metal–Organic Frameworks,' L. Liu, K. Konstas, M. R. Hill and S. G. Telfer, *J. Am. Chem. Soc.* **2013**, *135*, 17731.
13. 'Carbon Dioxide Capture in Metal–Organic Frameworks,' K. Sumida, D. L. Rogow, J. A. Mason, T. M. McDonald, E. D. Bloch, Z. R. Herm, T.-H. Bae and J. R. Long, *Chem. Rev.* **2012**, *112*, 724.
14. 'Methane Storage in Metal Organic Frameworks,' K. Konstas, T. Osl, Y. Yang, M. Batten, N. Burke, A. J. Hill and M. R. Hill, *J. Mater. Chem.* **2012**, *22*, 16698.
15. 'Topology of Interpenetration,' S. R. Batten, *CrystEngComm* **2001**, *3*, 67.
16. 'Interpenetrating Nets: Ordered, Periodic Entanglement,' S. R. Batten and R. Robson, *Angew. Chem., Int. Ed.* **1998**, *37*, 1460.
17. 'Topology, Chirality and Interpenetration in Coordination Polymers,' S.-Y. Zhang, Z. Zhang and M. J. Zaworotko, *Chem. Commun.* **2013**, *49*, 9700.
18. 'Interpenetration Control in Metal–Organic Frameworks for Functional Applications,' H.-L. Jiang, T. A. Makal and H.-C. Zhou, *Coord. Chem. Rev.* **2013**, *257*, 2232.
19. 'Interpenetrating Metal/Organic and Inorganic 3d Networks: A Computer-Aided Systematic Investigation. Part I. Analysis of the Cambridge Structural Database,' V. A. Blatov, L. Carlucci, G. Ciani and D. M. Proserpio, *CrystEngComm* **2004**, *6*, 378.
20. 'Interpenetrating Metal–Organic and Inorganic 3d Networks: A Computer-Aided Systematic Investigation. Part II [1]. Analysis of the Inorganic Crystal Structure Database (Icsd),' I. A. Baburin, V. A. Blatov, L. Carlucci, G. Ciani and D. M. Proserpio, *J. Solid State Chem.* **2005**, *178*, 2452.
21. 'Porous Materials with Optimal Adsorption Thermodynamics and Kinetics for Co<sub>2</sub> Separation,' P. Nugent, Y. Belmabkhout, S. D. Burd, A. J. Cairns, R. Luebke, K. Forrest, T. Pham, S. Ma, B. Space, L. Wojtas, M. Eddaoudi and M. J. Zaworotko, *Nature* **2013**, *495*, 80.
22. 'Effects of Functionalization, Catenation, and Variation of the Metal Oxide and Organic Linking Units on the Low-Pressure Hydrogen Adsorption Properties of Metal–Organic Frameworks,' J. L. C. Rowsell and O. M. Yaghi, *J. Am. Chem. Soc.* **2006**, *128*, 1304.
23. 'A Flexible Interpenetrating Coordination Framework with a Bimodal Porous Functionality,' T. K. Maji, R. Matsuda and S. Kitagawa, *Nat. Mater.* **2007**, *6*, 142.
24. 'Nonlinear Properties in Coordination Copolymers Derived from Randomly Mixed Ligands,' T.-H. Park, K. Koh, A. G. Wong-Foy and A. J. Matzger, *Cryst. Growth Des.* **2011**, *11*, 2059.
25. 'Control of Interpenetration for Tuning Structural Flexibility Influences Sorption Properties,' S. Bureekaew, H. Sato, R. Matsuda, Y. Kubota, R. Hirose, J. Kim, K. Kato, M. Takata and S. Kitagawa, *Angew. Chem., Int. Ed.* **2010**, *49*, 7660.
26. 'Interpenetration, Porosity, and High-Pressure Gas Adsorption in Zn<sub>4</sub>O(2,6-Naphthalene Dicarboxylate)<sub>3</sub>,' J. I. Feldblyum, D. Dutta, A. G. Wong-Foy, A. Dailly, J. Imirzian, D. W. Gidley and A. J. Matzger, *Langmuir* **2013**, *29*, 8146.
27. 'Framework-Catenation Isomerism in Metal–Organic Frameworks and Its Impact on Hydrogen Uptake,' S. Ma, D. Sun, M. Ambrogio, J. A. Fillinger, S. Parkin and H.-C. Zhou, *J. Am. Chem. Soc.* **2007**, *129*, 1858.
28. 'Enhanced Adsorption Selectivity of Hydrogen/Methane Mixtures in Metal–Organic Frameworks with Interpenetration: A Molecular Simulation Study,' B. Liu, Q. Yang, C. Xue, C. Zhong, B. Chen and B. Smit, *J. Phys. Chem. C* **2008**, *112*, 9854.
29. 'Photolabile Protecting Groups in Metal–Organic Frameworks: Preventing Interpenetration and Masking Functional Groups,' R. K. Deshpande, G. I. N. Waterhouse, G. B. Jameson and S. G. Telfer, *Chem. Commun.* **2012**, *48*, 1574.
30. 'Thermolabile Groups in Metal–Organic Frameworks: Suppression of Network Interpenetration, Post-Synthetic Cavity Expansion and Protection of Reactive Functional Groups,' R. K. Deshpande, J. L. Minnaar and S. G. Telfer, *Angew. Chem. Int. Ed.* **2010**, *47*, 4598.
31. 'Zinc-1,4-Benzenedicarboxylate-Bipyridine Frameworks - Linker Functionalization Impacts Network Topology During Solvothermal Synthesis,' S. Henke, A. Schneemann, S. Kapoor, R. Winter and R. A. Fischer, *J. Mater. Chem.* **2012**, *22*, 909.
32. 'Temperature and Concentration Control over Interpenetration in a Metal–Organic Material,' J. Zhang, L. Wojtas, R. W. Larsen, M. Eddaoudi and M. J. Zaworotko, *J. Am. Chem. Soc.* **2009**, *131*, 17040.



33. 'Actuation of Asymmetric Cyclopropanation Catalysts: Reversible Single-Crystal to Single-Crystal Reduction of Metal–Organic Frameworks,' J. M. Falkowski, C. Wang, S. Liu and W. Lin, *Angew. Chem.* **2011**, *123*, 8833.
34. 'Control of Framework Interpenetration for in Situ Modified Hydroxyl Functionalised Irmofs,' D. Rankine, A. Avellaneda, M. R. Hill, C. J. Doonan and C. J. Sumby, *Chem. Commun.* **2012**, *48*, 10328.
35. 'Transformation from Non- to Double-Interpenetration in Robust Cd(Ii) Doubly-Pillared-Layered Metal–Organic Frameworks,' H. Aggarwal, P. Lama and L. J. Barbour, *Chem. Commun.* **2014**, *50*, 14543.
36. 'Direct Evidence for Single-Crystal to Single-Crystal Switching of Degree of Interpenetration in a Metal–Organic Framework,' H. Aggarwal, P. M. Bhatt, C. X. Bezuidenhout and L. J. Barbour, *J. Am. Chem. Soc.* **2014**, *136*, 3776.
37. 'Reversible Interpenetration in a Metal–Organic Framework Triggered by Ligand Removal and Addition,' S. B. Choi, H. Furukawa, H. J. Nam, D.-Y. Jung, Y. H. Jhon, A. Walton, D. Book, M. O'Keeffe, O. M. Yaghi and J. Kim, *Angew. Chem., Int. Ed.* **2012**, *51*, 8791.
38. 'Temperature- or Guest-Induced Drastic Single-Crystal-to-Single-Crystal Transformations of a Nanoporous Coordination Polymer,' J.-P. Zhang, Y.-Y. Lin, W.-X. Zhang and X.-M. Chen, *J. Am. Chem. Soc.* **2005**, *127*, 14162.
39. 'Exploiting High Pressures to Generate Porosity, Polymorphism, and Lattice Expansion in the Nonporous Molecular Framework Zn(Cn)2,' S. H. Lapidus, G. J. Halder, P. J. Chupas and K. W. Chapman, *J. Am. Chem. Soc.* **2013**, *135*, 7621.
40. 'Systematic Design of Pore Size and Functionality in Isorecticular Mofs and Their Application in Methane Storage,' M. Eddaoudi, J. Kim, N. Rosi, D. Vodak, J. Wachter, M. O'Keeffe and O. M. Yaghi, *Science* **2002**, *295*, 469.
41. 'A General Thermolabile Protecting Group Strategy for Organocatalytic Metal–Organic Frameworks,' D. J. Lun, G. I. N. Waterhouse and S. G. Telfer, *J. Am. Chem. Soc.* **2011**, *133*, 5806.
42. 'The Reticular Chemistry Structure Resource (RCSR) Database of, and Symbols for, Crystal Nets,' M. O'Keeffe, M. A. Peskov, S. J. Ramsden and O. M. Yaghi, *Acc. Chem. Res.* **2008**, *41*, 1782.
43. Consistent with this, crystals formed at the onset of crystallization (reaction time of after eight hours) in straight DMF have a PIP level of 79%.
44. 'A Partially Interpenetrated Metal–Organic Framework for Selective Hysteretic Sorption Of carbon Dioxide,' S. Yang, X. Lin, W. Lewis, M. Suyetin, E. Bichoutskaia, J. E. Parker, C. C. Tang, D. R. Allan, P. J. Rizkallah, P. Hubberstey, N. R. Champness, K. M. Thomas, A. J. Blake and M. Schröder, *Nat. Mater.* **2012**, *11*, 710.
45. 'Structural Disorder in Molecular Framework Materials,' A. B. Cairns and A. L. Goodwin, *Chem. Soc. Rev.* **2013**, *42*, 4881.
46. 'On the Barrier to Inversion of Cyclooctatetraene. The Thermal Decomposition of Dibenzo[E,G][1,4]Diazocine,' N. L. Allinger, W. Szkrybalo and M. A. DaRooge, *J. Med. Chem.* **1963**, *28*, 3007.
47. 'Hierarchical Zeolites: Enhanced Utilisation of Microporous Crystals in Catalysis by Advances in Materials Design,' J. Perez-Ramirez, C. H. Christensen, K. Egeblad, C. H. Christensen and J. C. Groen, *Chem. Soc. Rev.* **2008**, *37*, 2530.
48. 'Mesoporosity--a New Dimension for Zeolites,' K. Moller and T. Bein, *Chem. Soc. Rev.* **2013**, *42*, 3689.
49. 'Chiral Drugs: An Overview,' L. A. Nguyen, H. He and C. Pham-Huy, *International Journal of Biomedical Science : IJBS* **2006**, *2*, 85.
50. 'Single-Crystal X-Ray Diffraction Studies on Structural Transformations of Porous Coordination Polymers,' J.-P. Zhang, P.-Q. Liao, H.-L. Zhou, R.-B. Lin and X.-M. Chen, *Chem. Soc. Rev.* **2014**, *43*, 5789.
51. 'Dimensionality Transformation through Paddlewheel Reconfiguration in a Flexible and Porous Zn-Based Metal–Organic Framework,' K. C. Stylianou, J. Rabone, S. Y. Chong, R. Heck, J. Armstrong, P. V. Wiper, K. E. Jelfs, S. Zlatogorsky, J. Bacsá, A. G. McLennan, C. P. Ireland, Y. Z. Khimiyak, K. M. Thomas, D. Bradshaw and M. J. Rosseinsky, *J. Am. Chem. Soc.* **2012**, *134*, 20466.
52. 'Transformation of a 1d to 3d Coordination Polymer Mediated by Low Temperature Lattice Solvent Loss,' A. S. R. Chesman, D. R. Turner, G. B. Deacon and S. R. Batten, *Chem. Commun.* **2010**, *46*, 4899.
53. 'Probing Microporous Materials with Second-Harmonic Generation.,' M. A. Van der Veen, T. Verbiest and D. E. De Vos, *Microporous Mesoporous Mater.* **2013**, *166*, 102.
54. 'Point Group Symmetry Determination Via Observables Revealed by Polarized Second-Harmonic Generation Microscopy: (1) Theory.,' M. A. Van der Veen, F. Vermoortele, D. E. De Vos and T. Verbiest, *Anal. Chem.* **2012**, *84*, 6378.
55. Note that variation in the SHG intensity for different crystals within the same image in Figure 4 is expected since the intensity of the signal depends on the orientation of the crystal with respect to the plane of polarization of the incident laser light.
56. MUF-10 was selected for this study in preference to MUF-9 since an asymmetric unit with a sufficiently small number of atoms to be amenable to DFT calculations can be generated.
57. 'Anisotropic Elastic Properties of Flexible Metal–Organic Frameworks: How Soft Are Soft Porous Crystals?,' A. U. Ortiz, A. Boutin, A. H. Fuchs and F.-X. Coudert, *Phys. Rev. Lett.* **2012**, *109*, 195502.

58. 'Investigating the Pressure-Induced Amorphization of Zeolitic Imidazolate Framework Zif-8: Mechanical Instability Due to Shear Mode Softening,' A. U. Ortiz, A. Boutin, A. H. Fuchs and F.-X. Coudert, *J. Phys. Chem. Lett.* **2013**, 4, 1861.
59. 'Thermal and Mechanical Stability of Zeolitic Imidazolate Frameworks Polymorphs,' L. Bouëssel du Bourg, A. U. Ortiz, A. Boutin and F.-X. Coudert, *APL Materials* **2014**, 2, 124110.
60. 'Metal–Organic Frameworks: Structural, Energetic, Electronic, and Mechanical Properties,' A. Kuc, A. Enyashin and G. Seifert, *The Journal of Physical Chemistry B* **2007**, 111, 8179.
61. 'Responsive Metal–Organic Frameworks and Framework Materials: Under Pressure, Taking the Heat, in the Spotlight, with Friends,' F.-X. Coudert, *Chem. Mater.* **2015**, 27, 1905.
62. 'Soft Porous Crystals,' S. Horike, S. Shimomura and S. Kitagawa, *Nat. Chem.* **2010**, 1, 695.
63. 'Flexible Metal–Organic Frameworks,' A. Schneemann, V. Bon, I. Schwedler, I. Senkowska, S. Kaskel and R. A. Fischer, *Chem. Soc. Rev.* **2014**, 43, 6062.
64. 'Dynamic Structural Transformations of Coordination Supramolecular Systems Upon Exogenous Stimulation,' C.-P. Li, J. Chen, C.-S. Liu and M. Du, *Chem. Commun.* **2015**, 51, 2768.
65. 'Mechanical Properties of Hybrid Inorganic–Organic Framework Materials: Establishing Fundamental Structure–Property Relationships,' J. C. Tan and A. K. Cheetham, *Chem. Soc. Rev.* **2011**, 40, 1059.
66. 'Route to a Family of Robust, Non-Interpenetrated Metal–Organic Frameworks with Pto-Like Topology,' N. Klein, I. Senkowska, I. A. Baburin, R. Grünker, U. Stoeck, M. Schlichtenmayer, B. Streppel, U. Mueller, S. Leoni, M. Hirscher and S. Kaskel, *Chem. Eur. J.* **2011**, 17, 13007.
67. 'Metal–Organic Frameworks with Wine-Rack Motif: What Determines Their Flexibility and Elastic Properties?,' A. U. Ortiz, A. Boutin, A. H. Fuchs and F.-X. Coudert, *J. Chem. Phys.* **2013**, 138, 174703.
68. 'Post-Synthetic Modification of Tagged Metal–Organic Frameworks,' A. D. Burrows, C. Frost, M. F. Mahon and C. Richardson, *Angew. Chem., Int. Ed.* **2008**, 47, 8482.
69. W. Ostwald, *Z. Phys. Chem.* **1897**, 22, 289.
70. 'Structural and Thermodynamic Explanations of Ostwald's Rule,' T. Threlfall, *Org. Process Res. Dev.* **2003**, 7, 1017.
71. 'Rational Design, Synthesis, Purification, and Activation of Metal–Organic Framework Materials,' O. K. Farha and J. T. Hupp, *Acc. Chem. Res.* **2010**, 43, 1166.
72. 'Amorphous Metal–Organic Frameworks,' T. D. Bennett and A. K. Cheetham, *Acc. Chem. Res.* **2014**, 47, 1555.